Letter

Purely viscous acoustic propulsion of bimetallic rods

Jeffrey McNeill,[1] Nathan Sinai,[1] Justin Wang,[1] Vincent Oliver,[1] Eric Lauga,[2] François Nadal,[3,*] and Thomas E. Mallouk[1,4]

[1]*Department of Chemistry, University of Pennsylvania, Philadelphia, Pennsylvania 19104-6323, USA*

[2]*Department of Applied Mathematics and Theoretical Physics, Centre for Mathematical Sciences, University of Cambridge, Wilberforce Road, Cambridge CB3 0WA, United Kingdom*

[3]*Wolfson School of Mechanical, Electrical and Manufacturing Engineering, Loughborough University, Loughborough LE11 3TU, United Kingdom*

[4]*International Centre for Materials Nanoarchitectonics (WPI-MANA), National Institute for Materials Science (NIMS), 1-1 Namiki, Tsukuba, Ibaraki 305-0044, Japan*

(Received 23 February 2021; accepted 2 August 2021; published 10 September 2021)

Synthetic microswimmers offer models for cell motility and their tunability makes them promising candidates for biomedical applications. Here, we measure the acoustic propulsion of bimetallic microrods that, when trapped at the nodal plane of a MHz acoustic resonator, swim with speeds of up to 300 μm s^{-1}. While past acoustic streaming models predict speeds that are more than one order of magnitude smaller than our measurements, we demonstrate that the acoustic locomotion of the rods is driven by a viscous, nonreciprocal mechanism relying on shape anisotropy akin to that used by swimming cells and that reproduces our data with no adjustable parameters.

DOI: 10.1103/PhysRevFluids.6.L092201

Biological and synthetic nano- and microswimmers operate at a low Reynolds number, and their study has been a place to discover and leverage new physics [1,2]. Since their introduction in 2004 [3], synthetic swimmers have been extensively studied, both to understand the fundamental physics of active fluids [4] and also for potential applications in biomedicine [5], materials science [6,7], environmental remediation [8], and analytical science [9]. These swimmers range in size from tens of nanometers to micrometers, and can be powered by catalysis [10], magnetic [11–13] and electric fields [14–16], light [17], ultrasound [18,19], or combinations thereof [20,21]. Interactions between swimmers lead to a rich variety of emergent behaviors, including self-assembly, chemotaxis, and spontaneous large-scale symmetry breaking [22–27]. Many of these powerful swimmers do not require toxic fuels and their compatibility with biological media enables applications in intracellular sensing and drug delivery [28–30].

The rapid propulsion of metallic microrods at the nodal plane of an acoustic standing wave was first discovered in 2012 [31]. Their electrochemical fabrication results in one end being concave and the other convex. With single-element rods, this shape asymmetry alone generates propulsion, but at relatively slow speeds compared to density-asymmetric bimetallic rods where the less dense end of the rod always leads [32]. The requirement for an asymmetry in shape or density is supported by experiments showing the locomotion of density-asymmetric spheres [33] and no directional propulsion for symmetric microrods [34]. Previous modeling proposed that the acoustic propulsion of metallic rods arises from the nonlinear inertial coupling between rotational and translational perturbation flows (acoustic streaming) [35–38]. However, this model has yet to reproduce experimental data quantitatively.

*f.r.nadal@lboro.ac.uk

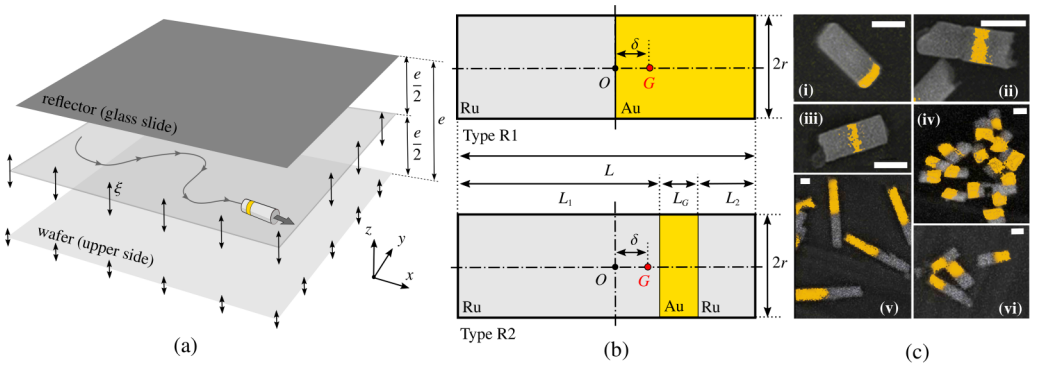

FIG. 1. (a) Diagram of the acoustic resonators. The amplitude of the acoustic field displacement at the pressure nodal plane is denoted by ξ so the corresponding transverse velocity is $\boldsymbol{U}_e = \xi\omega\exp(i\omega t)\hat{\boldsymbol{z}}$. (b) Geometry of the rods of types R1 and R2. The values of L, L_1, L_2, and L_G and corresponding standard deviations for type R2 are provided in the Supplemental Material [43]. (c) Scanning electron microscopy pictures of bimetallic rods: (i) type R2-A; (ii) type R2-B; (iii) type R2-C; (iv) type R1, $L = 587$ nm; (v) type R1, $L = 2458$ nm; (vi) type R1, $L = 990$ nm. The contrast between the gold stripe (yellow) and the ruthenium sections (gray) has been enhanced. In (c)(i)–(vi) the white scale bars are 300 μm long.

Here, we report experiments in which the density of multisegment bimetallic rods is varied along their length. Their forced propulsion in the nodal plane of an acoustic water-filled resonator is modeled by an unsteady viscous propulsion mechanism in which acoustic streaming plays no role. The amplitude of the forcing acoustic field is directly inferred from the drift dynamics of silica microspheres towards the pressure node [39]. The accurate measurement of the acoustic field displacement amplitude enables our model to reproduce the data with no adjustable parameters, making this, to the best of our knowledge, the first quantitative agreement with experiments on this phenomenon. Our model demonstrates that imbalanced microrods powered by ultrasound are, in fact, nonreciprocal Purcell motors, analogous in their undulatory swimming cycle to spermatozoa [40] and self-propelled viscous *flapping* swimmers [2,41,42].

Bimetallic microrods were fabricated by the electrodeposition of metals into the cylindrical, 300-nm-diameter pores of anodic aluminum oxide (AAO) membranes [31,32]. Two sets of rods (diameter $2r = 300$ nm, length L) were made [see Figs. 1(b) and 1(c)]: a first set of half-gold/half-ruthenium rods (type R1), with aspect ratio $\gamma = 2r/L$ made to vary by changing the total length L (average lengths $L = 384$, 587, 990, 1915, 2458, and 3921 nm); in the second set of rods (type R2), referred to as R2-A, R2-B, and R2-C (Au stripe at the end, in the second quarter of the rod, and in the middle, respectively), the distance δ between the centroid and center of mass was varied by changing the location of the gold stripe. Experimentally, the lengths of the second set of rods spanned from 539 to 1284 nm, with an average length $L = 892$ nm and a standard deviation $\Delta L = 164$ nm. The dimensions of the type R1 and type R2 rods are reported in the Supplemental Material [43].

The resonator cavity [see Fig. 1(a) and Supplemental Material [43]] was filled with de-ionized water (density ρ, dynamic viscosity η) seeded with microrods and a dilute suspension of 3-μm-diameter polystyrene or silica spheres. The first resonant mode frequencies, $f = \omega/(2\pi) = 2.17$, 3.17, 3.7, and 5.0 ± 0.15 MHz, were obtained by sweeping the frequency of the harmonic voltage source connected to the transducer, in the region corresponding to four gap thicknesses $e = 340$, 230, 195, and 150 ± 8 μm. In the following, the displacement amplitude of the transverse acoustic field at the pressure nodal plane is denoted by ξ so that the corresponding transverse velocity of the acoustic field is $\boldsymbol{U}_e = \xi\omega\exp(i\omega t)\hat{\boldsymbol{z}}$, with $\hat{\boldsymbol{z}}$ the unit vector in the z direction. Once the resonance frequency was found precisely, moving spheres were recorded rising to the pressure node when the ultrasound was turned on. The height and velocity of the tracer spheres could be inferred from

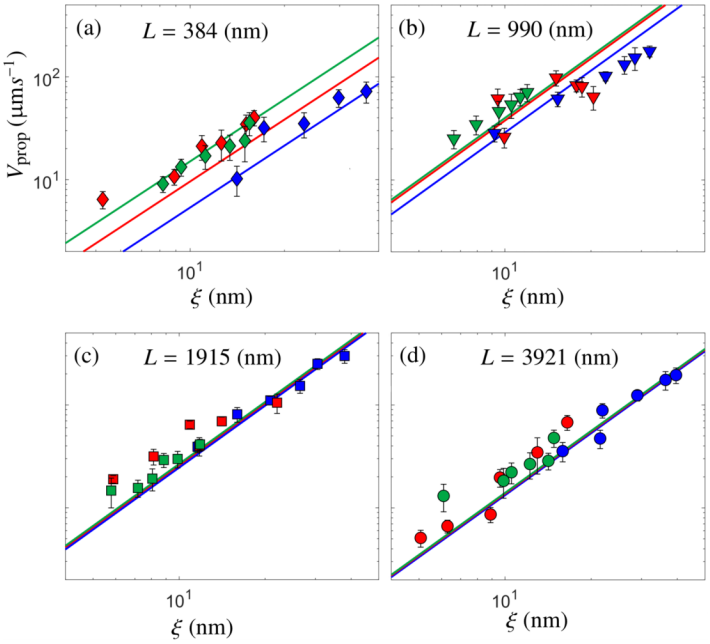

FIG. 2. (a)–(d) Propulsion speed of type R1 rods, V_{prop}, as a function of the acoustic displacement amplitude at the pressure nodal plane, ξ (nm), for four different rod lengths. The experimental data are plotted in solid symbols. The viscous model depicted in the text [Eq. (4)], for which $V_{prop} \sim \xi^2$, is shown in solid lines. Blue, red, and green symbols/lines correspond to the frequencies $f = 2.17$, 3.17, and 5.0 MHz, respectively.

the change in holographic halo diameter over time, (movie S1 [43]). Rods moving in the nodal plane (movie S2 [43]) were recorded for 5 s at 20 frames per second (FPS) (100 frames) and tracked using MOSAICSUITE with CLIJ GPU acceleration [44,45] in IMAGEJ [46] to capture ensemble velocities.

As in past work [31,32], the lighter end of the rods (Ru side) was always leading during locomotion (Fig. S1 in Supplemental Material [43]). The propulsion speed of the R1 rods, V_{prop}, is plotted in Fig. 2 as a function of the displacement amplitude ξ for four rod lengths and three forcing frequencies. The whole set of data can be fitted to a power law $V_{prop} \sim \xi^{1.75}$. The propulsion speed of R2 rods observed for a forcing frequency $f = 3.7$ MHz is shown in Fig. 3 as a function of the distance δ between the geometric center and the center of mass [see Fig. 1(b)]. As expected, V_{prop} is an increasing function of δ, which is the controlling symmetry-breaking parameter for type R2 rods. In the following, we show that the propulsion speed observed for both R1 and R2 rods can be reproduced quantitatively by a viscous mechanism in which only the inertia of the solid (and not the fluid) is accounted for.

Using a general dimensionless analysis, we see that the normalized acoustic propulsion speed of a rigid rod, $V_{prop}/(\xi\omega)$, depends on six dimensionless parameters [38]: the dimensionless asymmetry $\alpha = 2\delta/L$; the fluid-to-solid density ratio $\beta = \rho/\bar{\rho}$ ($\bar{\rho}$ being the mean density of the rod); the aspect ratio $\gamma = 2r/L$; the frequency Stokes parameter (which can be interpreted as the inverse of the dimensionless viscous diffusion length) $\lambda = (\rho r^2\omega/\eta)^{1/2}$; the dimensionless amplitude of the acoustic field at the pressure nodal plane $\varepsilon = \xi/r$; and the dimensionless inertia $\tilde{I} = I/I_h$ (I and I_h being the inertias of the original rod and that of the isovolume homogeneous rod about their respective centers of mass).

Past studies argued that the acoustic propulsion of metallic rods resulted from the nonlinear inertial coupling in the fluid between rotation and translation (phenomenon of so-called acoustic streaming). However, this physical mechanism has not been tested quantitatively, due to lack

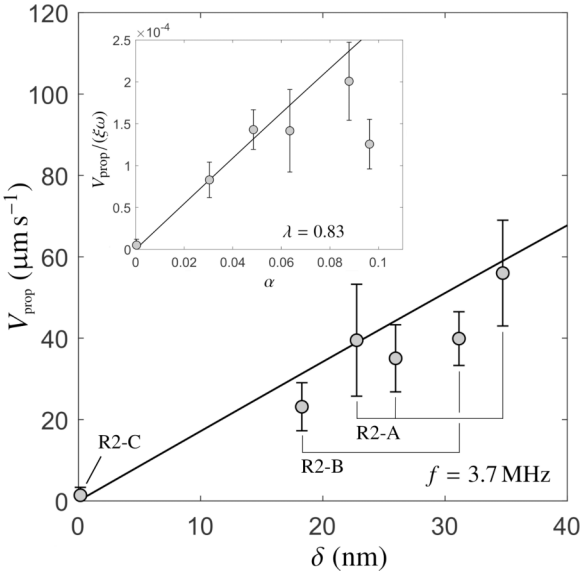

FIG. 3. Propulsion speed of type R2 rods, $V_{\rm prop}$ (μm s^{-1}), as a function of the asymmetry distance δ (nm), for $f = 3.7$ MHz. Due to fluctuations in the manufacturing process the length of type R2 rods lies in the range 539–1284 nm. The theory (viscous model) is plotted with a solid line for the mean value of the length $L = 892$ nm. Inset: Dimensionless form of the plot.

of knowledge of the local acoustic displacement amplitude. We used direct measurements of ξ and introduced reasonable values of the previously proposed dimensionless parameters in the available streaming-based predictive theories [35–38]. This led to quantitative predictions of the propulsion speed that underestimated the experimental values by more than one order of magnitude (see Supplemental Material [43]). The question therefore remains to determine the main physical mechanism governing acoustic propulsion. We argue here that the propulsion mainly results from the nonreciprocal (rectified) flapping motion of the rods, a viscous mechanism originally proposed in Ref. [47] for ellipsoids and illustrated in Fig. 4(b) (see the theoretical section below). In this

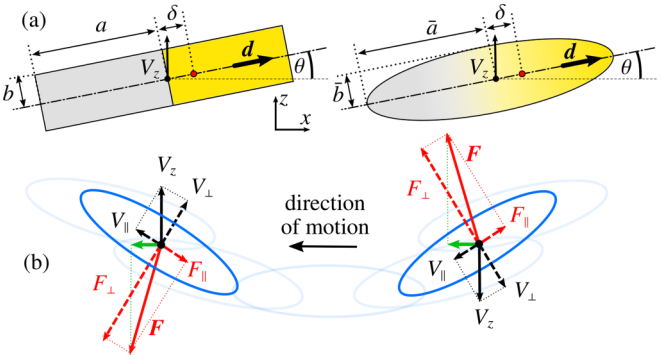

FIG. 4. (a) Equivalent ellipsoid model of the cylindrical rods used to derive an expression of the propulsion speed $V_{\rm prop}$. (b) Physical principle of the rectified viscous mechanism based on the combined effects of shape anisotropy and the flapping motion [47]. Regardless of the direction of the vertical velocity within a period of oscillation, the shape anisotropy yields a rectified force oriented towards the less dense end of the solid (green arrow).

mechanism, a propulsive force is created if a time-varying displacement of an elongated body (flapping) is combined with a time-varying change of conformation (angle) in a non-time-reversible fashion. To adapt these earlier results [47], we consider prolate spheroids of the same mass and aspect ratio [semiminor and major axis $\bar{b} = [3\gamma m/(4\pi\bar{\rho})]^{1/3}$ and $\bar{a} = \bar{b}/\gamma$—see Fig. 4(a)] whose flapping motion is forced by the transverse acoustic field. Note that this leads to a redefinition of the frequency parameter $\lambda = \bar{b}^2\omega/\nu$ and dimensionless amplitude $\varepsilon = \xi/\bar{b}$, which are now based on the semiminor axis $\bar{b}$, while the remaining dimensionless parameters are those of the initial rod. The averaged propulsion speed V_{prop} derived in Ref. [47] (where $\langle\cdot\rangle$ denotes the average over a period of oscillation) is

$$V_{\text{prop}} = \frac{\Lambda_\perp - \Lambda_\parallel}{\Lambda_\parallel}\langle V_z\,\theta\rangle, \tag{1}$$

from which one can infer that, in order to obtain a nonzero mean speed, (i) the local transverse (along the minor axis) and lengthwise (along the major-axis) Stokes drag coefficients $-6\pi\bar{a}\Lambda_\perp$ and $-6\pi\bar{a}\Lambda_\parallel$ must be different, and (ii) the vertical velocity V_z of the centroid (relative to the fluid) and the tilt angle θ of the major axis must not be $\pi/2$ out of phase from one another (otherwise the average would be zero). In order to compute the propulsion speed V_{prop}, we calculate the time-periodic quantities V_z and θ from Newton's laws by taking into account the inertia of the solid (only) [38]. We consider the incompressible limit in which the transverse dimensions of the rod are small compared to the acoustic wavelength. In this case, the forcing oscillatory flow can be approximated as locally uniform at the particle scale. In addition, ξ is assumed to be smaller than the minor axis of the rod, so $\varepsilon \ll 1$. We write the *imbalance* vector of the ellipsoid that results from its density asymmetry as $\boldsymbol{\delta} = \mathbf{OG} = \delta\,\boldsymbol{d}$, where $\boldsymbol{d}$ is the unit vector aligned with the major axis of the ellipse (Fig. 4). The conservation of momentum can be linearized in the small tilt angle limit ($\theta \ll 1$) as $\bar{\rho}\,\mathcal{V}\dot{\boldsymbol{V}} = m\,\boldsymbol{\delta}\times\ddot{\boldsymbol{\theta}} + \boldsymbol{F} + (\rho - \bar{\rho})\mathcal{V}\dot{\boldsymbol{U}}_e$, where $\ddot{\boldsymbol{\theta}} = \ddot{\theta}\,\hat{\boldsymbol{y}}$, $\boldsymbol{V} = V_z\hat{\boldsymbol{z}}$ is the oscillating velocity of the solid relative to the surrounding fluid, $\mathcal{V}$ is the volume of the particle, $\boldsymbol{F}$ is the corresponding viscous hydrodynamic force, and the last term is the effective buoyancy force. Similarly, the conservation of angular momentum can be written as $I\,\ddot{\boldsymbol{\theta}} = \boldsymbol{L} - \boldsymbol{\delta}\times(\boldsymbol{F} + \rho\mathcal{V}\dot{\boldsymbol{U}}_e)$, where $\boldsymbol{L} = -8\pi\bar{a}^3\Lambda_r\,\dot{\boldsymbol{\theta}}$ is the hydrodynamic torque about the (O, y) axis due to rotation. Using $\xi\omega$ and ω^{-1} as the reference velocity and timescale, and denoting by v_z the dimensionless velocity $V_z/(\xi\omega)$, yields the nondimensional forms of momenta conservation equations

$$\dot{v}_z = -\frac{A}{\varepsilon}\ddot{\theta} - B\,v_z + E\,e^{it}, \tag{2}$$

$$\ddot{\theta} = -C\,\dot{\theta} + \varepsilon D\,v_z - \varepsilon F\,e^{it}, \tag{3}$$

where $A = (\alpha/\gamma)$, $B = [(9\beta\Lambda_\perp/(2\lambda^2)]$, $C = [15\Lambda_r/(\lambda^2\tilde{I}\chi)]$, $D = [9\beta\Lambda_\perp/(2\lambda^2)]$, $E = i(\beta - 1)$, and $F = i[5\alpha\beta\gamma/(2\tilde{I}\chi)]$ do not depend on ε, since $\chi = (1+\gamma^2)/2$, $\Lambda_\parallel$, $\Lambda_\perp$, and Λ_r only depend on the aspect ratio of the rod. From Eqs. (2) and (3), it can be inferred that v_z and θ are $O(1)$ and $O(\varepsilon)$, respectively. So, writing these two quantities as $v_z = \hat{v}_0 e^{i\omega t}$ and $\theta = \varepsilon\,\hat{\theta}_0 e^{i\omega t}$, solving the system in Eqs. (2) and (3) for $\hat{v}_0$ and $\hat{\theta}_0$, and evaluating Eq. (1) leads to our theoretical prediction for the propulsion speed,

$$V_{\text{prop}} = \tfrac{1}{2}\xi\omega\,\varepsilon\,\text{Re}[\hat{\theta}_0^\dagger\hat{v}_0]. \tag{4}$$

The speed is thus of the form $V_{\text{prop}} = \xi\omega\,\varepsilon\,\mathcal{F}(\alpha, \beta, \gamma, \lambda, \tilde{I})$, where the dimensionless factor $\mathcal{F} = (1/2)\text{Re}[\hat{\theta}_0^\dagger\hat{v}_0]$ does not depend on ε, and is therefore proportional to the square of the forcing amplitude ξ. This quadratic dependence is close to the experimental scaling $V_{\text{prop}} \sim \xi^{1.75}$ obtained from a global least-squares fitting of the data (in Fig. 2, theory is plotted in solid lines).

The theoretical predictions are also shown in Fig. 3 in both dimensional and dimensionless forms. For small values of the asymmetry parameter α, one expects a linear dependence of the propulsion velocity with $V_{\text{prop}} = \xi\omega\,\varepsilon\,\alpha[\partial_\alpha\mathcal{F}]_{\alpha=0}$, as obtained. In both cases, the propulsion speed is quantitatively captured by the model, with no fitting parameters. The agreement includes both the

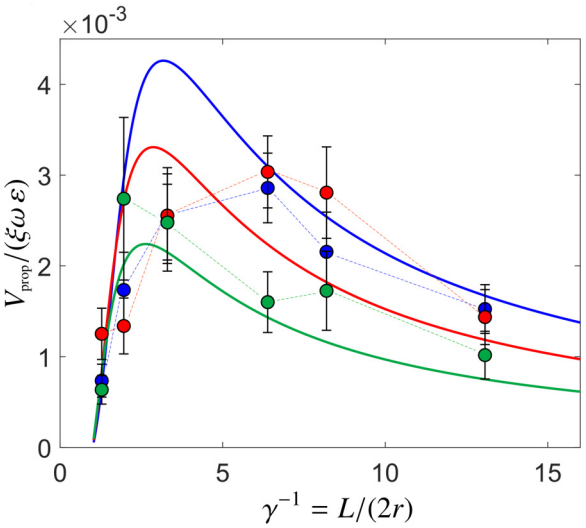

FIG. 5. Dimensionless propulsion velocity $V_{\text{prop}}/(\xi\omega)$ for type R1 rods rescaled by the dimensionless field amplitude ε. The experimental data are plotted in solid symbols; the theory is plotted in solid lines. The color code is the same as in Fig. 2.

direction of swimming (light end of the rod leading) and its magnitude. In Fig. 5, we next plot the dimensionless function $\mathcal{F}$ as a function of the inverse of the aspect ratio (dimensionless length) from the data in Fig. 2, by averaging the quantity $V_{\text{prop}}/(\xi\omega\varepsilon)$ over ε for each pair of parameters (λ, γ), i.e., for each pair of dimensioned parameters (f, L). Note that, for type R1 rods, $\mathcal{F}$ is a function of γ and λ only, since the values of the constants $\alpha \simeq 0.1$, $\beta \simeq 0.06$, and $\tilde{I} \simeq 1$ do not depend on the aspect ratio. Small discrepancies exist, e.g., the optimal length, which can be estimated from the measurements for $\lambda = 0.55$ and $\lambda = 0.67$ ($f = 2.17$ and 3.17 MHz), is underestimated by the model (at least by a factor of 2) and so is the corresponding value of function $\mathcal{F}$, but despite these, the model captures the major trends and orders of magnitude observed in the experimental data. In particular, the drop in propulsion velocity observed for $\gamma \to 1$ (due to the loss of anisotropy) agrees with the model, as is the decrease observed for $\gamma^{-1} \gg 1$, where axial drag becomes prominent.

In summary, we have presented here evidence that the acoustic propulsion of bimetallic cylindrical rods is driven by a viscous mechanism in which the fluid inertia plays no role. Mathematically, ignoring the inertia of the fluid is a valid assumption provided $\lambda^2 \ll 1$; in our experiments the values of λ^2 range from 0.3 to 0.7, and therefore our model remains quantitatively accurate even beyond the strict asymptotic limit in which it should be valid. Note that our model does not rule out contributions from other streaming-based mechanisms, which remain relevant in the case of pure spheres with strong imbalance [33]. The agreement between the model and our data with no fitting parameters strongly suggests that viscous flapping is the main mechanism governing the physics of acoustic propulsion of density-asymmetric metallic rods. Our work represents therefore a paradigm shift in our understanding of acoustic propulsion. With more detailed modeling and complex nanorod designs, a full description of this phenomenon should be within reach. These insights could inform the rational design of many different types of future nanoscopic swimmers and active matter powered by ultrasound and represent an important step towards a more holistic understanding of ultrasound-matter interactions and their nanoscale fluid dynamics, with a potential impact in biology, medicine, sensing, and fluid physics.

This project received funding from the European Research Council (ERC) under the European Union's Horizon 2020 research and innovation programme (Grant Agreement No. 682754

to E.L.). N.S. acknowledges Research Experiences for Undergraduates support under National Science Foundation Grant No. DMR-1952877. This work was carried out in part at the Singh Center for Nanotechnology, which is supported by the NSF National Nanotechnology Coordinated Infrastructure Program under Grant No. NNCI-2025608.

[1] E. Purcell, Life at low Reynolds number, Am. J. Phys. **45**, 3 (1977).
[2] E. Lauga and T. Powers, The hydrodynamics of swimming microorganisms, Rep. Prog. Phys. **72**, 096601 (2009).
[3] W. F. Paxton, K. C. Kistler, C. C. Olmeda, A. Sen, S. K. St. Angelo, Y. Cao, T. E. Mallouk, P. E. Lammert, and V. H. Crespi, Catalytic nanomotors: Autonomous movement of striped nanorods, J. Am. Chem. Soc. **126**, 13424 (2004).
[4] M. C. Marchetti, J.-F. Joanny, S. Ramaswamy, T. B. Liverpool, J. Prost, M. Rao, and R. A. Simha, Hydrodynamics of soft active matter, Rev. Mod. Phys. **85**, 1143 (2013).
[5] J. Wu, J. Troll, H.-H. Jeong, Q. Wei, M. Stang, F. Ziemssen, Z. Wang, M. Dong, S. Schnichels, T. Qiu, and P. Fischer, A swarm of slippery micropropellers penetrates the vitreous body of the eye, Sci. Adv. **4**, eaat4388 (2018).
[6] F. A. Lavergne, H. Wendehenne, T. Bäuerle, and C. Bechinger, Group formation and cohesion of active particles with visual perception-dependent motility, Science **364**, 70 (2019).
[7] C. Lozano, J. R. Gomez-Solano, and C. Bechinger, Active particles sense micromechanical properties of glasses, Nat. Mater. **18**, 1118 (2019).
[8] Y. Ying and M. Pumera, Micro/nanomotors for water purification, Chem. - Eur. J. **25**, 106 (2019).
[9] Y. Wang, C. Zhou, W. Wang, D. Xu, F. Zeng, C. Zhan, J. Gu, M. Li, W. Zhao, J. Zhang, J. Guo, H. Feng, and X. Ma, Photocatalytically powered matchlike nanomotor for lightguided active SERS sensing, Angew. Chem., Int. Ed. **57**, 13110 (2018).
[10] X. Ma, A. Jannasch, U.-R. Albrecht, K. Hahn, A. Miguel-López, E. Schäffer, and S. Sánchez, Enzyme-powered hollow mesoporous Janus nanomotors, Nano Lett. **15**, 7043 (2015).
[11] W. Gao, S. Sattayasamitsathit, K. Manian Manesh, D. Weihs, and J. Wang, Magnetically powered flexible metal nanowire motors, J. Am. Chem. Soc. **132**, 14403 (2010).
[12] H. Xie, M. Sun, X. Fan, Z. Lin, W. Chen, L. Wang, L. Dong, and Q. He, Reconfigurable magnetic microrobot swarm: Multimode transformation, locomotion, and manipulation, Sci. Robot. **4**, eaav8006 (2019).
[13] R. Dreyfus, J. Baudry, M. Roper, M. Fermigier, H. Stone, and J. Bibette, Microscopic artificial swimmers, Nature (London) **437**, 862 (2005).
[14] J. Yan, M. Han, J. Zhang, C. Xu, E. Luijten, and S. Granick, Reconfiguring active particles by electrostatic imbalance, Nat. Mater. **15**, 1095 (2016).
[15] J. Zhang, J. Yan, and S. Granick, Directed self-assembly pathways of active colloidal clusters, Angew. Chem., Int. Ed. **128**, 5252 (2016).
[16] M. Z. Bazant and T. M. Squires, Induced-Charge Electrokinetic Phenomena: Theory and Microfluidic Applications, Phys. Rev. Lett. **92**, 066101 (2004).
[17] M. Xuan, Z. Wu, J. Shao, L. Dai, T. Si, and Q. He, Near infrared light-powered Janus mesoporous silica nanoparticle motors, J. Am. Chem. Soc. **138**, 6492 (2016).
[18] D. Ahmed, T. Baasch, B. Jang, S. Pane, J. Dual, and B. Nelson, Artificial swimmers propelled by acoustically activated flagella, Nano Lett. **16**, 4968 (2016).
[19] J. M. McNeill, N. Nama, J. M. Braxton, and T. E. Mallouk, Wafer-scale fabrication of micro- to nanoscale bubble swimmers and their fast autonomous propulsion by ultrasound, ACS Nano **14**, 7520 (2020).
[20] B. Dai, J. Wang, Z. Xiong, X. Zhan, W. Dai, C. C. Li, S. P. Feng, and Tang, Programmable artificial phototactic microswimmer, J. Nat. Nanotechnol. **11**, 1087 (2016).
[21] C. Chen, F. Mou, L. Xu, S. Wang, J. Guan, Z. Feng, Q. Wang, L. Kong, W. Li, J. Wang, and Q. Zhang, Lightsteered isotropic semiconductor micromotors, Adv. Mater. **29**, 1603374 (2017).

[22] J. Palacci, S. Sacanna, A. Preska-Steinberg, D. J. Pine, and P. M. Chaikin, Living crystals of light-activated colloidal surfers, Science **339**, 936 (2009).
[23] Y. Hong, N. M. K. Blackman, N. D. Kopp, A. Sen, and D. Velegol, Chemotaxis of Nonbiological Colloidal Rods, Phys. Rev. Lett. **99**, 178103 (2007).
[24] A. Somasundar, S. Ghosh, F. Mohajerani, L. Massenberg, T. Yang, P. Cremer, D. Velegol, and A. Sen, Positive and negative chemotaxis of enzyme-coated liposome motors, Nat. Nanotechnol. **14**, 1129 (2019).
[25] A. Sokolov, I. S. Aranson, J. O. Kessler, and R. E. Goldstein, Concentration Dependence of the Collective Dynamics of Swimming Bacteria, Phys. Rev. Lett. **98**, 158102 (2007).
[26] J. R. Howse, R. A. L. Jones, A. J. Ryan, T. Gough, R. Vafabakhs, and R. Golestanian, Self-Motile Colloidal Particles: From Directed Propulsion to Random Walk, Phys. Rev. Lett. **99**, 048102 (2007).
[27] D. P. Singh, A. Domínguez, U. Choudhury, S. N. Kottapalli, M. N. Popescu, S. Dietrich, and P. Fischer, Interface-mediated spontaneous symmetry breaking and mutual communication between drops containing chemically active particles, Nat. Commun. **11**, 2210 (2020).
[28] W. Wang, S. Li, L. Mair, S. Ahmed, T. Huang, and T. Mallouk, Acoustic propulsion of nanorod motors inside living cells, Angewandte Chemie **53**, 3201 (2014).
[29] B. Esteban-Fernàndez de Ávila, C. Angell, F. Soto, M. Angel Lopez-Ramirez, D. F. Báez, S. Xie, J. Wang, and Y. Chen, Acoustically propelled nanomotors for intracellular siRNA delivery, ACS Nano **10**, 4997 (2016).
[30] B. Esteban-Fernàndez de Ávila, D. E. Ramírez-Herrera, S. Campuzano, P. Angsantikul, L. Zhang, and J. Wang, Nanomotor-enabled pH-responsive intracellular delivery of Caspase-3: Toward rapid cell apoptosis, ACS Nano **11**, 5367 (2017).
[31] W. Wang, L. Castro, M. Hoyos, and T. Mallouk, Autonomous motion of metallic microrods propelled by ultrasound, ACS Nano **6**, 6122 (2012).
[32] S. Ahmed, W. Wang, L. Bai, D. Gentekos, M. Hoyos, and T. Mallouk, Density and shape effects in the acoustic propulsion of bimetallic nanorod motors, ACS Nano **10**, 4763 (2016).
[33] M. Valdez-Garduño, M. Leal-Estrada, E. Oliveros-Mata, D. Sandoval-Bojorquez, F. Soto, J. Wang, and V. Garcia-Gradilla, Density asymmetry driven propulsion of ultrasound-powered Janus micromotors, Adv. Funct. Mater. **30**, 2004043 (2020).
[34] C. Zhou, L. Zhao, M. Wei, and W. Wang, Twists and turns of orbiting and spinning metallic microparticles powered by megahertz ultrasound, ACS Nano **11**, 12668 (2017).
[35] F. Nadal and E. Lauga, Asymmetric steady streaming as a mechanism for acoustic propulsion of rigid bodies, Phys. Fluids **26**, 082001 (2014).
[36] K. Lippera, O. Dauchot, S. Michelin, and M. Benzaquen, No net motion for oscillating near-spheres at low Reynolds numbers, J. Fluid Mech. **866**, R1 (2019).
[37] J. Collis, F. Jesse, D. Chakraborty, and J. Sader, Autonomous propulsion of nanorods trapped in an acoustic field, J. Fluid Mech. **825**, 29 (2017).
[38] F. Nadal and S. Michelin, Acoustic propulsion of a small bottom-heavy sphere, J. Fluid Mech. **898**, A10 (2020).
[39] R. Barnkob, P. Augustsson, T. Laurell, and H. Bruus, Measuring the local pressure amplitude in microchannel acoustophoresis, Lab Chip **10**, 563 (2010).
[40] E. A. Gaffney, K. Ishimoto, and B. J. Walker, Modelling Motility: The Mathematics of Spermatozoa, Front. Cell Dev. Biol. **9**, 1927 (2021).
[41] L. Becker, S. Koehler, and H. Stone, On self-propulsion of micro-machines at low Reynolds number: Purcell's three-link swimmer, J. Fluid Mech. **490**, 15 (2003).
[42] M. Shelley and J. Zhang, Flapping and bending bodies interacting with fluid flows, Annu. Rev. Fluid Mech. **43**, 449 (2011).
[43] See Supplemental Material at http://link.aps.org/supplemental/10.1103/PhysRevFluids.6.L092201 for information about the method of measurement of the acoustic field amplitude, the method of fabrication of the rods resonators, the direction of propulsion of the rods, and orders of magnitudes obtained from the different models available in the literature. The captions of the movie files S1 and S2 are also provided in the SM.

[44] R. Haase, L. Royer, P. Steinbach, D. Schmidt, A. Dibrov, U. Schmidt, M. Weigert, N. Maghelli, P. Tomancak, F. Jug, and E. Myers, CLIJ: GPU-accelerated image processing for everyone, Nat. Methods **17**, 5 (2020).

[45] I. Sbalzarini and P. Koumoutsakos, Feature point tracking and trajectory analysis for video imaging in cell biology, J. Struct. Biol. **151**, 182 (2005).

[46] J. Schindelin, I. Arganda-Carreras, E. Frise, V. Kaynig, M. Longair, T. Pietzsch, S. Preibisch, C. Rueden, S. Saalfeld, B. Schmid, J. Tinevez, D. White, V. Hartenstein, K. Eliceiri, P. Tomancak, and A. Cardona, Fiji: An open-source platform for biological-image analysis, Nat. Methods **9**, 676 (2012).

[47] L. Was and E. Lauga, Optimal propulsive flapping in Stokes flows, Bioinspir. Biomim. **9**, 016001 (2014).